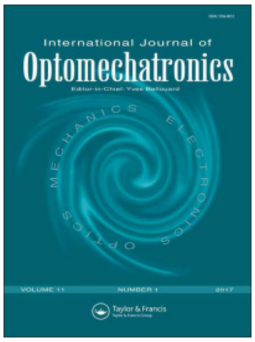

Taylor & Francis
Taylor & Francis Group

International Journal of Optomechatronics

ISSN: 1559-9612 (Print) 1559-9620 (Online) Journal homepage: www.tandfonline.com/journals/uopt20

Rapid deep-learning-based optical measurement of printed linear structures

Maxim Polomoshnov, Nowab Reza MD Ashif, Klaus-Martin Reichert, Aziza El Hariry, Ulrich Gengenbach, Ingo Sieber & Markus Reischl

To cite this article: Maxim Polomoshnov, Nowab Reza MD Ashif, Klaus-Martin Reichert, Aziza El Hariry, Ulrich Gengenbach, Ingo Sieber & Markus Reischl (2026) Rapid deep-learning-based optical measurement of printed linear structures, International Journal of Optomechatronics, 20:1, 2598112, DOI: 10.1080/15599612.2025.2598112

To link to this article: https://doi.org/10.1080/15599612.2025.2598112

INTERNATIONAL JOURNAL OF OPTOMECHATRONICS
2026, VOL. 20, NO. 1, 2598112
https://doi.org/10.1080/15599612.2025.2598112

Taylor & Francis
Taylor & Francis Group

Rapid deep-learning-based optical measurement of printed linear structures

Maxim Polomoshnov, Nowab Reza MD Ashif, Klaus-Martin Reichert, Aziza El Hariry, Ulrich Gengenbach, Ingo Sieber and Markus Reischl

Institute for Automation and Applied Informatics, Karlsruhe Institute of Technology (KIT), Eggenstein-Leopoldshafen, Germany

ABSTRACT
Conventional optical measurement techniques are beneficial in automated manufacturing processes due to their fast and non-intrusive operation. However, they require sophisticated and expensive equipment as well as increased personnel qualification. While the integration of machine learning contributes to alleviating these requirements, it needs a time-consuming and tedious preparation of training datasets. We introduce a twin concept to conduct rapid measurement of various geometrical properties of printed lines using deep learning. For the first time, a tedious collection and assessment of training data is substituted by synthetic generation of digital samples, which enables flexible, fast, and precise data processing. A full-field analysis of a non-preprocessed image conducted by a neural network facilitates measurement of multiple geometrical properties of an object at once. Corresponding network architecture, workflows, and metrics are outlined. The application area of the concept is demonstrated, but not limited to the field of functional printing. The method can easily be tailored to a wide range of engineering fields.

KEYWORDS
Optical measurement; process automation; deep learning; machine learning; computer vision; neural network; quality assurance

1. Introduction

State-of-the-art production processes, such as micro and nano fabrication, additive or advanced manufacturing, or high-throughput applications, require fast and contactless assessment of various characteristics of the outcomes. Among them, geometrical and functional properties of a fabricated product are the most essential.[1–3] Optical metrology responds to such demand, but remains cautious about application of novel machine-learning (ML) approaches.[2–5] Despite their faster and less complicated workflow, which is a crucial factor in manufacturing, ML-based measurements are expected to be less accurate and less reliable compared to the classic measurement techniques.[1,2,4,5] Hence, a ML-based measurement procedure demands new insights into principles of its utilization, to comply with metrological standards.[2,3,5] We address this issue to better understand applicability of ML-assisted optical measurements of geometric parameters by means of a synthetic training dataset.

In the first section, we portray the state of the art in the related field, briefly discuss identified problems, and introduce key terms and definitions. Section 2 proposes a twin concept to bridge identified gaps. Furthermore, data preparation, workflow, and metrics are described. The results obtained are presented in Section 3 and discussed in detail in Section 4. In Section 5, we summarize the outcome of the paper, propose the potential transfer to further application areas, and highlight avenues for the potential future work.

CONTACT Maxim Polomoshnov maxim.polomoshnov@kit.edu Institute for Automation and Applied Informatics, Karlsruhe Institute of Technology (KIT), Eggenstein-Leopoldshafen, Germany.

Nomenclature

ML	Machine learning	ε	Accuracy variance
DL	Deep learning	SF	Smoothness factor
CV	Computer vision	L (index)	Label values
NN	Neural network	M (index)	Measured values
CNN	Convolutional neural network	H	Image height
IJP	Inkjet printing	W	Image width
DIW	Direct-ink writing	B_n, B_m	Image baselines
2D, 3D	2-dimensional, 3-dimensional	E_n, E_m	Edge functions
ROI	Region of interest	b	Background color
V	Output variable	f	Foreground color
X	Mean line width	λ	Wavelength-to-image-height ratio
Y	Standard Deviation of corresponding X	r	Gaussian blur radius
Y_M^{corr}	Standard Deviation corrected with respect to the measurement error	P	Estimated proportion
		I-IV	Measurement methods I-IV
SD	Standard deviation	α	Scale factor
MAPE	Mean absolute percentage error	ReLU	Rectified Linear Unit
acc	Accuracy	Conv2D	2D-Convolutional layer
acc_{WS}	Weighted accuracy	BaychNorm2D	2D Batch normalization layer

1.1. Inkjet printing and direct-ink writing

Both inkjet printing (IJP) and direct-ink writing (DIW) are additive manufacturing techniques, which enable a structured multi-layer deposition of materials based on a digitally-generated printing layout.[6–9] Both technologies are able to use a wide range of materials, such as polymers, metals, nanoparticles, ceramics, biomaterials, etc.,[6–9] and find application in different engineering fields (e.g., 3D printing,[6,8] microelectronics,[1,8–10] biomedical,[6,8] material,[7,8] optical,[11] and textile[8,9] engineering). For IJP, liquid inks with a low viscosity ($\ll$100 mPa·s) are typical, which results upon ejection by an actuator in the formation of tiny single droplets with a minor load of a functional material.[7,9] Adjacent deposited droplets coalesce in lines and form a thin layer with a desired layout.[7,9,12] Extrusion-based DIW is capable of processing highly-viscous pastes ($\gg$1 Pa·s) so a continuous formation of a thick-layer line with a high load of a functional material takes place.[8,9] Then, individual lines fuze into a required 3D structure. Thus, both IJP and DIW single-nozzle systems produce linear traces, which form more complex printed structures.[6–8,10] Although optical measurement of such lines directly while printing is beneficial for immediate quality control, it is currently severely limited.[1,8,13] We propose the integration of ML-supported measuring into the printing process to facilitate its further automation and quality improvement, along with a reduction of waste.

1.2. Optical metrology and computer-vision based measurements

Optical metrology encompasses a plurality of contact-free methods and processes that use light as an information carrier to measure object properties and physical quantities.[14,15] Among others, interferometry, diffraction, holography, and light scattering are commonly used to assess geometrical, dimensional, textural, structural, or physical properties of a fabricated item to be probed (*object*).[5,14–16] In computer vision (CV), *digitization* of an object via optical sensors generates a digital-data array (*object image*)[5,16–18] that is correlated with the object appearance and, hence, reflects its visible properties.[18–21] Conventional optical measurement technology demands additional use-case dependent enhancements of the collected image: rectification, denoising, normalization, gradient reduction, binarization, etc.[5,20,22] Such data transformations are able to jeopardize accuracy and reliability of the object.[5,18,20,21,23] To tackle this issue, increased hardware and set-up requirements emerge (e.g., laser modules are frequently utilized as a light source to improve image quality).[5,14,16,18,20,21,23–25] For instance, in the field of printed microelectronics, intricate multilayer objects with thin transparent layers and indistinct shapes are typical. Namely, a transparent layer containing extraneous inclusions, a field-effect transistor, and a sensor with interdigitated electrodes are exemplarily shown in

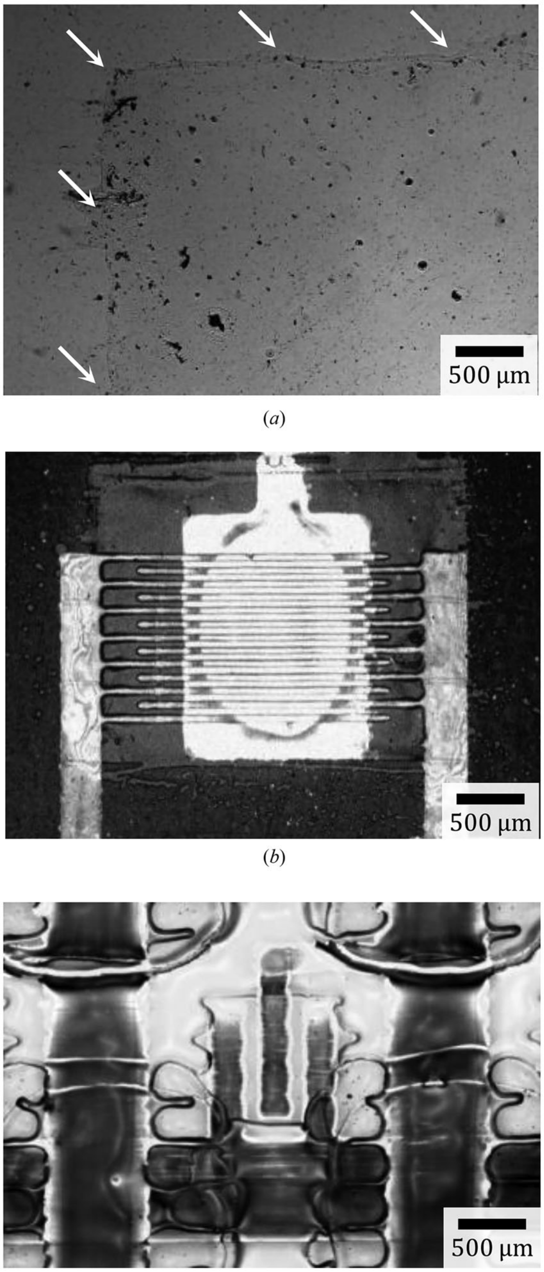

(*a*)

(*b*)

(*c*)

Figure 1. Examples of inkjet-printed objects from the field of microelectronics, requiring a rigorous manual property assessment in the case of common CV-based measurement techniques. (*a*) Thin transparent layer with extraneous inclusions and an indistinct edge, marked with arrows. (*b*) Multilayer field-effect transistor, comprising transparent and reflective layers, and intricate interdigitated electrodes. (*c*) Multilayer chemical sensor, comprising highly-uneven transparent insulating layers, and crossing and interdigitated electrodes.

Figure 1. Such objects demand rigorous manual operations to assess them correctly via CV-based techniques.

Integration of ML methods into CV measurement systems enables fully-automatic data processing with high flexibility and no human interaction. In this case, object positioning and data collection occur solely via optical sensors. Since there is no demand for specialized equipment and manual operations, the approach is considered to be simple, inexpensive, and not human-bias prone. A high degree of automation facilitates rapidity and variety of measurements. However, the output accuracy remains unproven.[1,3,5,22,26,27]

1.3. Machine learning

ML constructs an elaborated statistical prediction model to link input and output data automatically and efficiently.[4,5,19,27] Deep learning (DL) is an enhanced technique of ML using multilayer neural networks (NN).[2,5,28] During NN training, optimization of model parameters occurs through their successive adjustment on training data that include both input and reference output (*label*) values.[2,27,28] An optimized model has a minimal discrepancy between the label and the actual output values.[1,4,5]

A vast amount of different NN architectures has been developed in the recent years.[2,3,5,27–29] Among them, convolutional NNs (CNN) are preferred to extract and analyze image features to classify or assess represented objects.[1–3,22,28,29] Its simple architecture enables fast training, but has difficulties with low-quality input data, such as low-contrast and noisy images, or insufficient input-data variation.[1,3,22,28] The major disadvantage of the DL approach is the need to collect a large, well-balanced training dataset.[1,4,5,19,22,27,29]

1.4. Related work

Literature study revealed a keen and growing interest in the integration of precise ML-based measurement techniques into various engineering fields beyond printing, such as metrology,[4,22,30] agriculture,[31] health care,[28,32] construction engineering,[33–36] mechanical manufacturing,[2,5] additive manufacturing,[13,37] and microfabrication.[3,38] Conventional measurement procedures place high demands on equipment and on image quality to acquire accurate data, and require manual operations.[1,2,5,25,33]

Holm et al. discussed applicability of CV and ML methods for an automatic microstructural analysis, and demonstrated their high potential in the practical field.[38] Vallejo et al. identified a gap in the representation and comprehension of available and required training data, which challenges application of ML-based methods in soft metrology.[4] Chai et al. and Mahadevkar et al. systematized application scenarios of ML and DL in CV systems.[19,27] Fan et al. revealed a higher level of uncertainty for the ML-based indirect measurement methods in the field of nanomanufacturing, compared to the slower physics-based approach.[26] Tercan and Meisen indicated an increasingly important role of ML and DL models for quality prediction in manufacturing, pointed out central challenges in their application, and suggested application of synthetic training data instead of the natural ones.[2] Tin et al. demonstrated applicability of a CNN model to predict and classify wafer-overlay errors in a semiconductor fabrication process.[39] Roach et al. implemented a DL-based approach to optimize process parameters into a real-time monitoring of a DIW-3D-printing process, using a CV pipeline.[13] Shabani and Martinez-Hernandez employed a deep NN for an instant image segmentation and contour detection to measure filament width *in-situ* in a 3D-printing process.[37]

Carrasco et al. developed a CV-based method to measure surface-crack width with a high precision, overperforming DL-segmentation techniques.[33] Lamouchi et al. integrated DL into crack-width estimation to inspect concrete structures.[34] Tang et al. proposed an improved algorithm to measure crack width, combining DL-based image segmentation with subsequent contour refining and pixel counting.[36] Nyathi et al. employed a DL-based image segmentation and subsequent skeletonization to detect and measure concrete cracks with support of a novel laser calibration method.[35] Ponnusamy et al. combined a DL-segmentation model with a pixel calculation to compute joint-space widths from hand-radiograph images.[32] Liang et al. utilized image skeletonization and ML for a real-time measurement of cut tobacco with a low error rate.[31] Baderot et al. built a DL model and developed a tool to identify, classify, and measure objects from scanning and transmission electron microscopy objects *via* an accurate image segmentation.[22] Kuzin et al. indicated specific requirements for a successful integration of ML technologies into metrological practice.[30] Xue et al. investigated integration of ML into optical metrology, identified potential efficiency and effectiveness improvements in the field through ML, and highlighted existing challenges to be solved.[40]

To summarize, the following challenges were reported by researchers:

a. ML and DL techniques are mostly utilized in CV systems for image enhancement, classification, and segmentation, and for contour detection. Subsequent pixel counting to measure object dimensions occurs without employment of ML.[13,19,27,33,34,36,37]

b. ML-based approaches have not yet demonstrated any measurement accuracy, comparable to the traditional methods.[2,4,5,26,33]

c. DL methods need a well-developed training dataset, assembling of which is a long-lasting and onerous process that has to be repeated for each trial. Production-process limits additionally obstruct preparation of such datasets.[1,2,4,5,19,27,39,40]

d. Specific input-image requirements for industrial applications remain not considered yet.[2,3,5,31,34,36,39]

2. Methods

The present section introduces a novel twin concept uniting (a) a concept of measurement of multiple diverse geometrical values directly from a raw object image, based on the ML probability estimation, and (b) a concept of substitution of the real-data training dataset by a digitally-generated one, including images and their precise geometrical properties. The related data and their collection workflows, NN architecture and workflow, and metrics to assess accuracy of the twin concept are specified.

2.1. Proposed twin concept

Currently, ML and DL applications are mostly limited to an automatic enhancement, masking, and contouring in traditional image processing, and are sufficient for object classification. Figure 2 shows a schematic representation of the conventional application of DL and ML methods in image processing (depicted by the red-dashed frame) in comparison with our proposed method (depicted by the green-dashed frame). Following the workflow of the conventional approach, after *digitization*, each *raw object image* has to be subsequently *enhanced* to improve its quality, *masked* to distinguish regions of interest (ROI), and *contoured* to identify object edges. For measurement of geometric properties, the *pixel number* in the ROI has to be counted and scaled by *image resolution R* to obtain a quantified *target measurand* (in Figure 2: X_1). Hence, an incorrect edge detection directly causes an invalid value of the target measurand. Moreover, such measurements are usually limited to a single measurand. All input images have to be strictly adjusted to the dataset format, and ML/DL algorithms tailored for specific ROIs. To this extent, the amount of supplementary manual work multiply increases, with a sharp reduction in algorithm accuracy and versatility.

We proposed to use DL techniques to quantify multiple measurands with an appropriate accuracy directly from the raw object image, simplifying and speeding up the procedure (green-dashed frame in Figure 2). Using a *raw object image* as input, a *NN* is aimed to issue a probability for each *predefined*

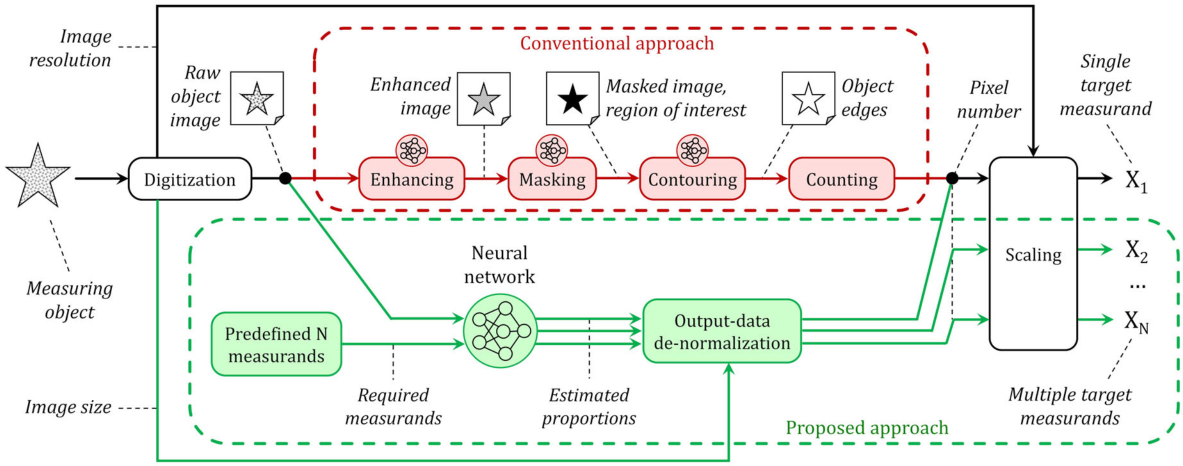

Figure 2. Schematic representation of the proposed measurement concept based on direct data acquisition from the raw full-field object image, and subsequent analysis via neural network (green-dashed frame). Conventionally, the image has to be processed in a sequence of steps, possibly assisted by tailored neural networks (red-dashed frame), which requires additional effort and jeopardizes measurement accuracy.

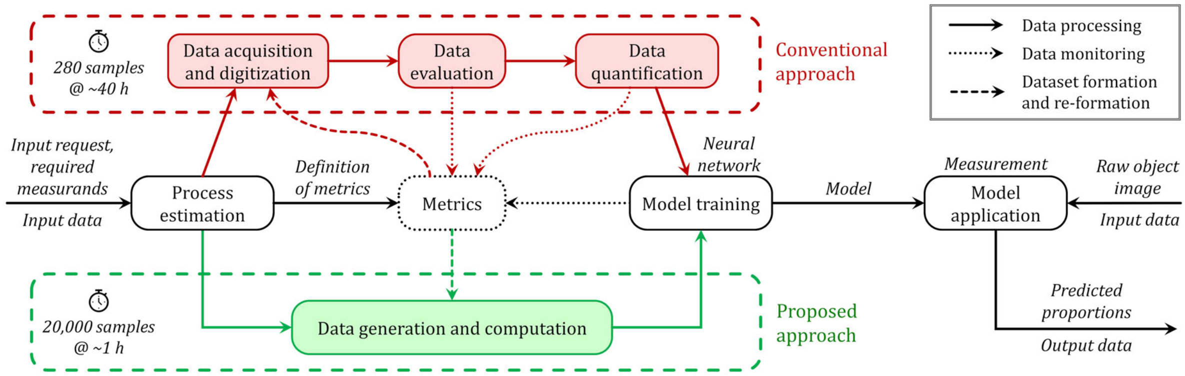

Figure 3. Schematic representation of the proposed concept based on rapid training-data generation. Instead of the conventional data collection and assessment that are highly labor-intensive and onerous (red-dashed frame), synthetic training data and simultaneously computed label data have to be utilized (green-dashed frame). Time spent in this work at collecting the specified amount of data samples is indicated for illustration.

measurand in the range between 0 and 1. After *de-normalization* via *image size*, and re-scaling via *image resolution*, quantified values of N multiple *target measurands* become obtained (in Figure 2: X_2 to X_N). However, a challenging collection and labeling of the training set is required before the model training. This workflow, schematically depicted in Figure 3, red-dashed frame, includes acquisition of a large number of object samples, their digitization, tedious evaluation, and quantification of the resulting data, to collect sufficient training data. In each stage, data fitness to predefined metrics has to be monitored. If required, samples have to be re-collected (i.e., re-fabricated) to ensure their variety and quality. In particular, the collection of 280 natural samples addressed in this study lasted about 40 h.

In our approach (Figure 3, green-dashed frame), we integrated a fully-controllable preparation of digitally-generated (*synthetic*) data samples that substituted real-world (*natural*) object samples. Recently, a similar approach has been suggested in the field of biophysics to accelerate training-data preparation, and to intensify laboratory automation. It did not consider geometric accuracy of the measured values (see Refs.[29,41,42]). A synthetic dataset is beneficial since it does not demand supplementary evaluation and quantification steps. Corresponding values become simultaneously computed with high precision during data generation. Digital re-generation of an unsatisfactory dataset is rapid and flexible. As indicated in Figure 3, generation of 20,000 training samples used in this work lasted 55 min, and, hence, is more than 3400 times faster than in the conventional approach.

Thus, the proposed twin concept offers four major advantages:

a. flexibility in the type and amount of measurands, pre-set during the NN training;
b. identification of implicit measurands (such as standard deviation of the measuring values) due to the full-field image analysis;
c. simplification and acceleration of the measurement process due to reduction in its auxiliary stages; and
d. substantial increase in process automation.

2.2. Data and dataset collection

In this pilot study, two types of plain printed lines, IJP and DIW, were inspected to validate the approach. For training purposes, a synthetic dataset was prepared. Simplistic synthetic images were designed not to resemble images of real printed lines in detail, but to address their distinctive features. The main focus was on identification of the line widths and their variance, with the target accuracy of 90% or more. For simplification, the length of the lines was not considered.

2.2.1. Target measurands

For natural reasons, printed lines tend to spread periodically over the substrate surface, and do not have a constant width at the microscale, important for microfabrication. Hence, two quantities were

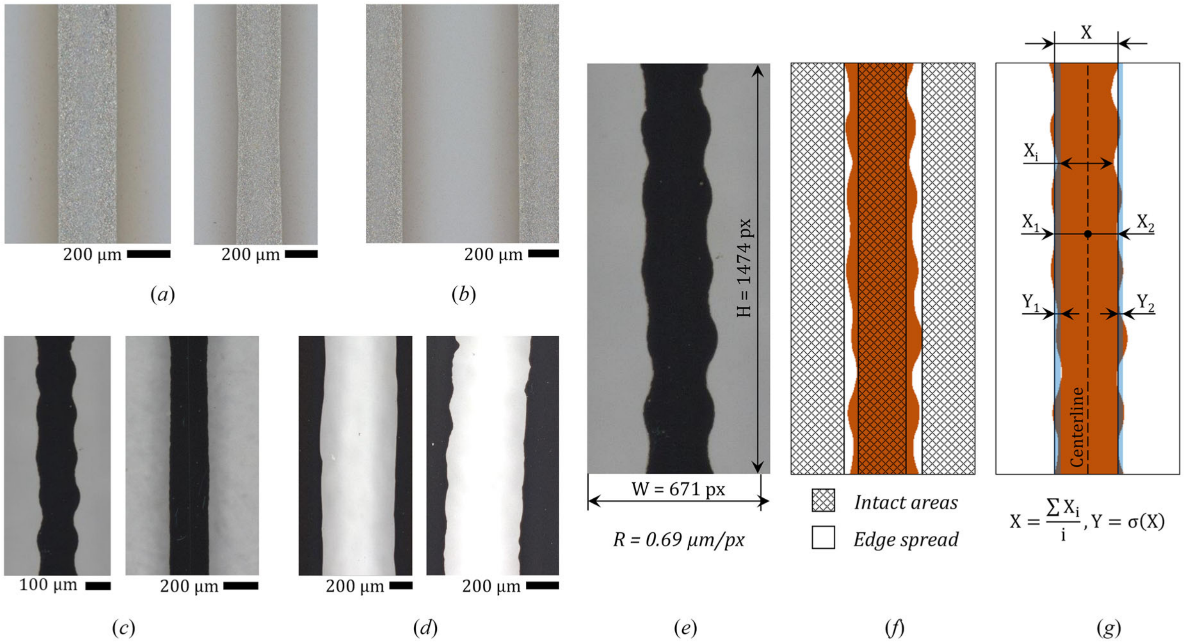

Figure 4. Natural data. Exemplary (*a*,*b*) direct-ink-written and (*c*,*d*) inkjet-printed lines. (*a*,*c*) single lines, (*b*,*d*) corresponding interline spaces. (*e*) Exemplary input data: image, digital dimensions *H* and *W*, and resolution *R* (not indicated $X_L = 144.59\,\mu\text{m}$, $Y_L = 16.09\,\mu\text{m}$). (*f*) Edge-spread areas, relevant for the base effect in the measurement accuracy for *Y*, and irrelevant areas, remaining intact during data acquisition. (*g*) Target measurands (*X*: mean line width, *Y*: *SD* of *X*, as a measure of the line-width variance) and their geometrical meaning.

selected to be measured: (a) the *mean line width X [µm]*, and (b) its *standard deviation Y [µm]* as a measure of the line-width variance. Thus, the ultimate representation of the measurement result was $X \pm Y$ *[µm]*. Each X and Y were attributed with two values: reference *label values* X_L *and* Y_L, and *measured values* X_M *and* Y_M, identified by the model from a raw line image.

2.2.2. Natural data

71 IJP and 71 DIW lines were fabricated and digitized. The samples were printed on polyimide, polyethylene terephthalate, and ceramic substrates using silver and carbon-based inks and pastes. For each type, 70 lines and 70 interline spaces were saved as individual images with different sizes, 280 data in total. Five image resolutions R were considered in the range 0.345 to 2.083 µm/px. Interline spaces were included to test algorithm versatility on perplexing images. Hence, each image consisted of three zones, as exemplarily presented in Figures 4(*a*)–(*d*): the foreground linear structure in the middle of the image, and two identical background zones beside. Each line was measured 10 to 20 times via optical microscopy to collect label data. Resulting images were augmented (mirrored in both directions, rotated by 180°, and randomly gamma corrected in the range 0.5 to 1.5) five times to form a dataset of 1400 labeled images.[43,44] Input data related to each collected image (*viz.* digital image size in [px], image resolution R in [µm/px], and label values X_L and Y_L in [µm]) are exemplarily shown in Figure 4(*e*). Edge-spread areas relevant to Y, and areas remaining intact during data acquisition are indicated in Figure 4(*f*). Target measurands X and Y, and their geometrical meaning are illustrated in Figure 4(*g*).

Since $Y \ll X$, narrow edge-spread areas, depicted in Figure 4(*f*), cause a *base effect*, which has to be considered when processing the results. The base effect is a mathematical effect, commonly used in economics and statistics.[45] It refers to the choice of a basis for comparison between data points that affects a large variation in ratio or percentage. A disproportionately small or large basis causes misrepresentation of the comparison result, reflected in seemingly abnormal ratio values.[45,46] Natural-data collection lasted ∼40 h in total (IJP: 1 h printing-data preparation, 1 h printing-process preparation, 1 h fabrication; DIW: 1.5 h printing-process preparation, 18.5 h fabrication; 0.5 h sample collection, 15 h optical microscopy and value calculation, 1 h data labeling).

2.2.3. Synthetic data

For image synthetization, an image generator was programmed in Python. The image size was 100×500 px with a conditional resolution $R = 1$ µm/px. Two provisional straight *baselines* B_n and B_m were generated, forming a simple three-zone model, depicted in Figure 5(*a*). The maximum distance between the baselines was 5% to 90% of the image width. The back and foreground areas had a solid fill of a random brightness ("*color*") in the range 0% (color value 0) to 100% (color value 255). The absolute color difference determined image contrast. The *contrast level* was calculated as the image contrast divided by 255. To avoid NN ambiguity, the minimum contrast level was limited by 0.2.

Motivated by the natural dataset, we distinguished between three major types of edge shapes: straight, periodic, and aperiodic edges. This partition was enhanced by dividing periodic edges into low-frequency ($1 \leq \lambda \leq 0.2$, where λ is the ratio of the wavelength in pixel to the image height) and high-frequency ($0.1 \leq \lambda \leq 0.01$). Also, a *no-line* type without any explicit pattern was added to avoid a false-positive identification of linear structures in low-contrast images (i.e., by color differences ≤ 4). As

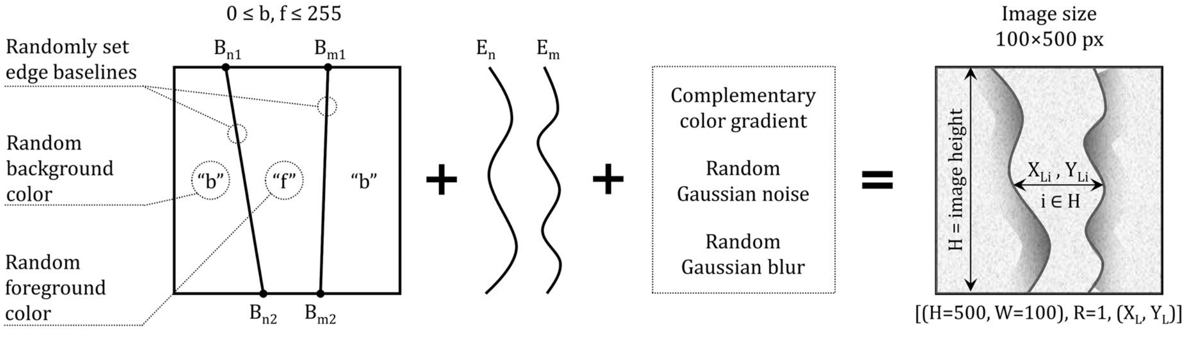

(*a*) (*b*) (*c*) (*d*)

Figure 5. Schematic representation of the image-generation principle. (*a*) Primary image of a three-zone linear structure with two straight baselines B_n and B_m, and two random colors b and f. (*b*) Generation and application of complementary edge functions E_n and E_m, in accordance with the edge class. (*c*) Generation and application of factors increasing algorithm robustness. (*d*) Ultimate synthetic image and related data: digital image size, conditional resolution, and two label values X_L and Y_L.

Table 1. Edge classes.

Class	0	1	2	3	4
Number of generated images	2000	4500	4500	4500	4500
Class description	Empty images without any explicit lines	Lines with straight-line edges	Lines with low-frequency periodic edges	Lines with high-frequency periodic edges	Lines with aperiodic rough edges
Schematic representation	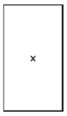		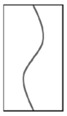	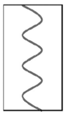	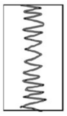
Range of values for X_L and Y_L	$X_L = Y_L = 0$	$X_L > 0$, $Y_L \geq 0$	$X_L > 0$, $Y_L > 0$		
Exemplary synthetic image and related label data $X_L \pm Y_L$ [px]	 0.00 ± 0.00	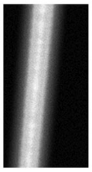 23.22 ± 1.77	 13.97 ± 3.03	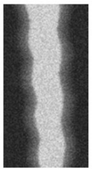 38.00 ± 5.68	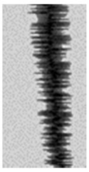 27.98 ± 12.73
Exemplary state of a printing process or affecting factors	Clogged printing nozzle, printing failure, extremely high or low wetting	Normal printing process, ideal printed line	Insufficient substrate heating, excessive printing resolution, ink spreading	Excessive substrate heating, insufficient printing resolution	Rough substrate, damaged printed line, unstable droplet generation (satellite droplets)

a result, five *edge classes* were defined, described, and exemplified in Table 1. Initially, 4000 images per class were generated. Then, the amount of the no-line samples (class 0) was reduced by half due to their sameness, and equally distributed for other classes to retain the total amount of 20,000 images in the dataset.[43]

As shown in Figure 5(*b*), two *edge functions* E_n and E_m were randomly generated for each image and class, and added to the relating baselines. Gradient colors mimicking natural-line thickness were randomly added to each generated image, as indicated in Figure 5(*c*). Each image was enhanced by random Gaussian noise and blur to improve model robustness during training. Gaussian noise was generated as a separate noise layer ($\mu = 128$, $\sigma = 128$) and combined with the image layer with a factor between 0 and 0.2, denominated *noise level*. Gaussian blur ($0 \leq r \leq 2$) was randomly applied to the finished image. Resulting synthetic image and related image data (*viz.* digital image size 100×500 px, image resolution $R = 1\ \mu\text{m/px}$, and label values X_L and Y_L in [px]) are schematically represented in Figure 5(*d*).

Since line edges in synthetic images were set via explicit equations, each image pixel was unambiguously related to either back or foreground area. Hence, the distance between edge functions E_n and E_m was definable numerically, by subtracting in each *pixel row i* (see Figure 5(*d*)). That allowed us to compute and arrange required label values X_L and Y_L automatically, directly during image generation. In total, 20,000 synthetic images were generated and labeled within 55 min.

2.2.4. Measurement accuracy

As known from metrology[16,24,47] and noticed in[4,5,22] the true measurand values are never completely undoubted. Hence, on the natural dataset, conducted measurements to collect reference label values were expected to contain a measurement error that had to be considered further. To address the error, we manufactured additional IJP and DIW samples, and asked three independent experts to measure them using one of the following methods and equipment:

a. manually (i.e., CV-based, with a large number of manual operations) with a digital microscope (*M I*),
b. semi-automatically (i.e., CV-based, with few manual operations) with an optical profilometer (*M II*),
c. automatically (i.e., CV-based, without any manual operations) with an optical probe station (*M III*).

The scheme, number, and accuracy of measurements were left to the experts' discretion to avoid any authors' influence on the measurement results. Upon measurements, discrepancies between three methods were quantified pairwise, and the total congruence among three methods was found as the mean error (Equations 1a and 1b).

$$Congruence(X_{M\ I}, X_{M\ II}, X_{M\ III}) = 1 - \frac{\sum_i^{IJP,\,DIW}[\varepsilon_i(I,II), \varepsilon_i(II,III), \varepsilon_i(I,III)]}{6}, \tag{1a}$$

where *error* ε is an accuracy variance for two particular methods A and B:

$$\varepsilon(A,B) = 1 - \frac{\min(X_{M\ A}, X_{M\ B})}{\max(X_{M\ A}, X_{M\ B})}, X_{M\ A}, X_{M\ B} > 0. \tag{1b}$$

Afterwards, the same two samples were measured using the proposed DL-based algorithm (*M IV*), the results were compared with the experts' ones to define their joint congruence (Equation 1c).

$$Congruence(X_{M\ IV}) = 1 - \frac{\sum_i^{IJP,\,DIW}[\varepsilon_i(I,IV), \varepsilon_i(II,IV), \varepsilon_i(III,IV)]}{6}. \tag{1c}$$

2.3. Neural-network architecture and workflow

In our previous work,[1] a plain CNN was demonstrated to be able to assess multiple functional properties of printed samples directly from their images. At the outset, in the present work, we tailored the algorithm as indicated in Figure 6. No pre-processing of the raw input images was conducted. As the first step, the *input image data* were loaded as three-channel images, rescaled to 256×256 px, and normalized via the *OpenCV* library (ver. 4.10.0) to obtain a data array $image^*$ with pixel values in the range [0, 1]. The *scale factor* α equal to the image width divided by 256 px was kept for the later data de-normalization. The data array was encoded eight times, using 2D convolution, 2D batch normalization, and the *ReLU* activation functions. The resulting $1 \times 1 \times 1024$ data array was flattened and operated in the *fully-connected layers*, consisting of four linear and three ReLU activation functions. Corresponding to the amount of predefined measurands, two bounded output regressands were ranged to [0, 1] with the *sigmoid* function. In the present study, the regressands are designated as *estimated proportions* P_X and P_Y, representing proportion of the evaluated dimension to the image size. The sigmoid function acted as an easily differentiable and smooth output filter. To reduce its potential saturation, all linear layers were initialized before the model training as follows: the weights were uniformly distributed in the range $\left[-1/\sqrt{y}; 1/\sqrt{y}\right]$, where y is the number of input features; the biases were equaled to 0.01. For the same reason, generated training images had a limited baseline distance (see Figure 5(*a*)) to avert training data near range limits. Thereby, design of the synthetic images determined the threshold value. As a result, sigmoid input was supposed not to reach extremes. Finally, the values were de-normalized to [px] using the scale factor α, and re-scaled to [µm] using *resolution R* of the input image data. Thus, *output data* encompassed values of the desired measurands X_M and Y_M.

A batch of eight images was utilized for the model training, test and validation were performed on single images. The mean squared error (L2) between the output data X_M, Y_M, and the label data X_L, Y_L,

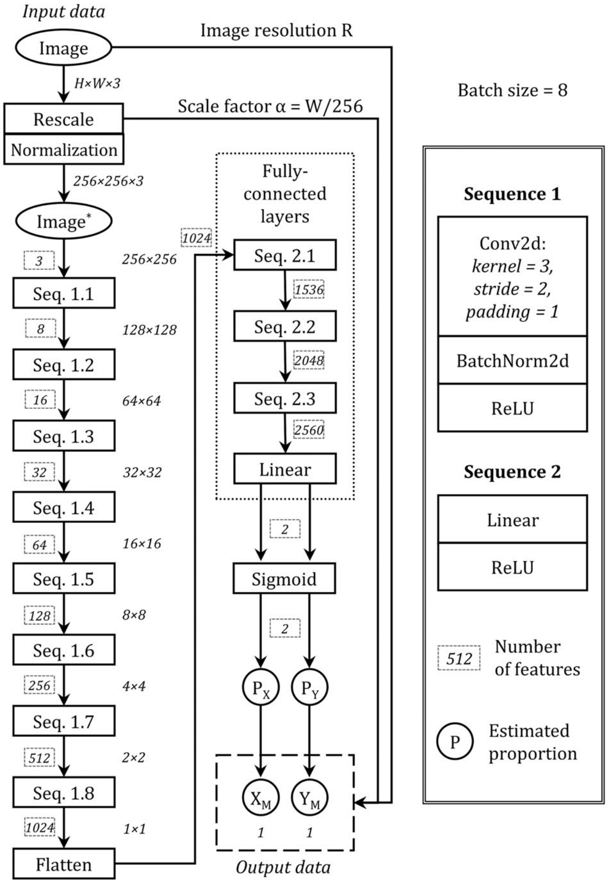

Figure 6. The neural-network architecture.

multiplied by an empirically-found constant factor $\lambda = 1000$, was used as loss function. The learning-rate scheduler was composed of four step-based cycles (36, 18, 12, and 9 epochs, 75 in total) with a sinusoidal reduction by half within each cycle. The initial learning rate was set as 2×10^{-4}. Before model training, the complete synthetic dataset was divided into a training, a validation, and a test set (95, 2.5, and 2.5%, respectively) using the *Random Split* method. After each epoch, validation on synthetic dataset was conducted. The natural dataset was not utilized during model training and validation. After each training epoch, the model was tested on the complete natural dataset to monitor training process on real data. Upon complete training, the model was tested on both synthetic and natural datasets separately to obtain results to be assessed. All experiments were repeated 10 times to estimate algorithm inaccuracy.

2.4. Metrics

To assess algorithm outcomes, for each *output variable V* (i.e., X or Y), its measurement accuracy *acc(V)* was found using Equations 2a–b.[1] Thus, *acc(V)* represented measurement uncertainty dependent on the *label value* V_L—see range of values in Table 1. For a positive V_L, Equation 2a was applied, so accuracy was defined as a min-to-max ratio between V_L and the *measured value* V_M. For a V_L equal to zero, a ratio between V_M and the image size was considered, according to Equation 2b. The resulting accuracy does not exceed 100% that means a complete match of V_M and V_L:

$$acc(V) = \left[\begin{array}{ll} \dfrac{\min(V_L, V_M)}{\max(V_L, V_M)}\cdot 100\%, & V_L > 0 \\ \left(1 - \dfrac{V_M}{image\ size\ [\mu m]}\right)\cdot 100\%, & V_L = 0 \end{array}\right. , 0 \le acc(V) \le 100\%. \qquad \begin{array}{r}(2a)\\(2b)\end{array}$$

Since such measurement accuracy is not conventional in the standard metrology practice, the mean absolute percentage error (MAPE) was employed as a subsidiary metric (Equation 3):

$$MAPE(V) = \frac{1}{n}\cdot\sum_{i=1}^{n}\frac{|V_{Li} - V_{Mi}|}{V_{Li}}\cdot 100\%, V_L > 0. \tag{3}$$

To unify X and Y as a single value, required for a simplified evaluation of the measurement results, *weighted accuracy* acc_{WS} was found as a weighted sum of their particular accuracy values (Equation 4):[1]

$$acc_{WS} = \frac{acc(X)\cdot X_L + acc(Y)\cdot Y_L}{X_L + Y_L}\cdot 100\%, X_L > 0. \tag{4}$$

The *measurement error* ε was the deviation of the accuracy from 100% (Equation 5).

$$\varepsilon = 100\% - acc. \tag{5}$$

We expected measurement errors to be positive. Under such circumstances, resulting Y values do not conform to a proper standard deviation and have to be corrected. Therefore, *standard deviations corrected with respect to the measurement errors* Y_M^{cor} were estimated (Equation 6).

$$Y_M^{cor} = \sqrt{Y_M^2 + [Y_M\cdot\varepsilon(Y)]^2 + [X_M\cdot\varepsilon(X)]^2}. \tag{6}$$

To avert the base effect when interpreting acc(Y) values, we estimated the *smoothness factor SF* (Equation 7), which is a measure of vicinity between the ratios Y_M^{cor}/X_M and Y_L/X_L. Lines with a lower SF value tend to have smoother edges, and, hence, to be more affected by the base effect:

$$SF = 1 - \sqrt{\left(\frac{Y_M^{cor}}{X_L} - \frac{Y_L}{X_L}\right)^2 + \left(\frac{Y_L}{X_M} - \frac{Y_L}{X_L}\right)^2}, X_L, X_M > 0. \tag{7}$$

2.5. Equipment

The digital microscope *Keyence VHX-7000* was employed for optical microscopy. A 3D profilometer *Sensofar S neox* was utilized for optical profilometry. An in-house built automatic probe station, equipped with a grayscale area-scan camera *acA2040-35gm* (*Basler*) and a brightfield back/coaxial forward illumination was used as an optical probe station.[48] An image binarization was implemented in the measurement algorithm of the probe station, with a potential impact on measurement accuracy.

The training, validation, and testing of the established NN were performed on a machine with 128 GB of RAM, two 18-core processors Intel Xeon Gold 6354, and four GPUs NVidia GA102GL (RTX A6000) with 48 GB VRAM (driver version 555.42, CUDA version 12.5). The machine was operated by the 64-bit operating system Ubuntu 22.04.4 LTS. 8 CUDA workers were utilized for all ML processes. The programming was carried out in Python 3.12.8 and PyTorch 2.5.0.

3. Results

Each synthetic image was generated within ∼165 ms. Training duration of the model was 113.4 s ± 0.9 s per epoch, which corresponds to 6.0 ms/(epoch·image). The completely pre-trained model required ∼140 ms for assessment of a single image.

On the synthetic test dataset, the total measurement accuracy reached 86.9% for the line width X, and 82.3% for its standard deviation Y. In addition, a slight variation among classes was found, as shown in Table 2. With an increase in the edge roughness (classes 1–4), accuracy for X decreased from 88.5 to 83.1%. Simultaneously, accuracy for Y grew from 74.8 to 92.0%. For empty images (class 0), corresponding accuracies of 88.2 and 76.1% were comparable with the ones for straight lines (class 1). With the mean synthetic-line width of 23.0 px and spread of 7.2 px, the corresponding measurement errors were 2.7 ± 1.0 and 1.1 ± 0.2 px.

The training process demonstrated a fast convergence, as can be seen from Figure 7(*a*) (blue line). Negligible decreases in the loss value, induced by the employed learning-rate scheduler (dashed green line), are distinguishable upon 14th, 42nd, 57th, and 72nd epochs. Training accuracy reached a plateau after ∼30 epochs (grey line). Thereafter, only a minor improvement in the results was noticed. Validation on the synthetic (red line) and the natural (yellow line) showed a similar development, with a plateau after ∼50 epochs, caused by a small learning-rate value. During validation, an average difference to the training accuracy was 1.7 percentage point less for synthetic images and 4.0 percentage points more for natural data. The latter was caused by more contrast real images with less noise and blur, compared to the training dataset of synthetic images.

On the natural dataset, in the aggregate, the assessed line width X_M was similar to the reference value X_L for both line types, as indicated in Figure 7(*b*). Corresponding accuracy acc(X) attained 92.6% for all lines (91.2% for DIW, 94.0% for IJP). Respective MAPE(X) scores were 9.2, 11.2, and 7.1%. However, the line-width variance Y_M was estimated significantly higher in respect to the reference values Y_L. Thus, acc(Y) attained 43.1% in total (26.3% for DIW, 60.0% for IJP). MAPE(Y) scores were 342.0, 586.1, and 97.9%, correspondingly. Since DIW lines had highly smooth edges (see Figures 4(*a*) and (*b*)), they were expected to be heavily affected by the base effect, in contrast to IJP lines. The obtained results correlated well with the smoothness factor SF that was smaller for DIW lines, and with the measurement accuracy on synthetic data (see Table 2: acc(Y) for classes 1–3). Despite seemingly low acc(Y) values and huge MAPE(Y) scores, the weighted accuracy acc_{WS} was comparable with acc(X): 91.7% for all lines, 90.6% for DIW, and 92.8% for IJP, due to the minor impact of overestimated, but still small Y values.

A more thorough comparison of the measured and label values (without consideration of augmented natural samples) revealed for DIW lines a greater deviation of the *line width X* from the *ideal match*

Table 2. Mean measurement accuracy on the synthetic test dataset, $n = 5000$.

Class	0	1	2	3	4	All
acc(X) [%]	88.23 ± 0.48	88.46 ± 2.36	87.65 ± 1.95	87.85 ± 1.04	83.14 ± 1.50	86.92 ± 0.36
acc(Y) [%]	76.10 ± 0.35	74.80 ± 1.05	80.80 ± 1.36	84.31 ± 1.47	91.97 ± 0.53	82.28 ± 0.60

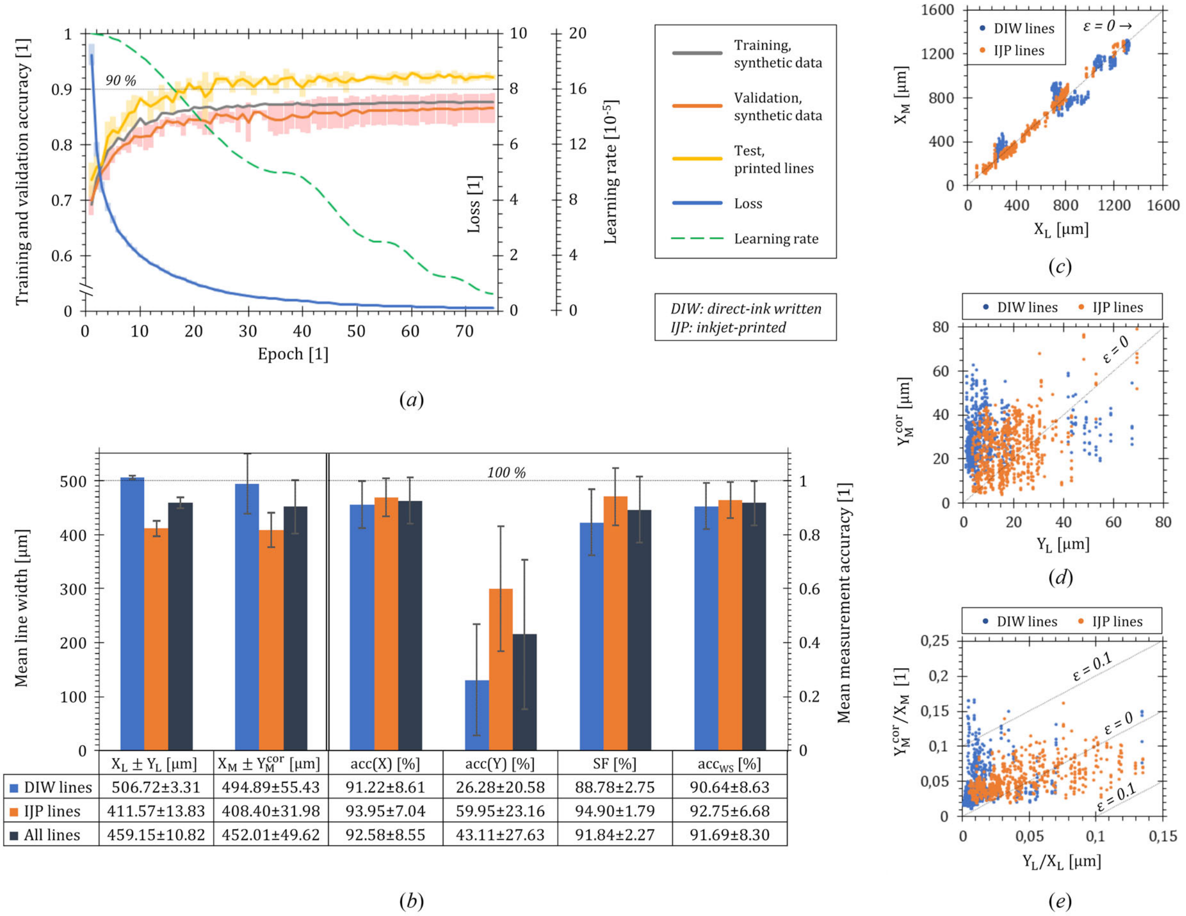

(*a*)

	$X_L \pm Y_L$ [μm]	$X_M \pm Y_M^{cor}$ [μm]	acc(X) [%]	acc(Y) [%]	SF [%]	acc_{WS} [%]
■ DIW lines	506.72±3.31	494.89±55.43	91.22±8.61	26.28±20.58	88.78±2.75	90.64±8.63
■ IJP lines	411.57±13.83	408.40±31.98	93.95±7.04	59.95±23.16	94.90±1.79	92.75±6.68
■ All lines	459.15±10.82	452.01±49.62	92.58±8.55	43.11±27.63	91.84±2.27	91.69±8.30

(*b*)

(*c*)

(*d*)

(*e*)

Figure 7. (*a*) Mean training and validation accuracy during model training, $n = 10$. Pale bars indicate the standard error. (*b*) Mean measurement accuracy on the natural dataset via the proposed algorithm, depending on the printed-line type, $n = 2000$. (*c*) Measured line widths *X*, (*d*) corresponding corrected *SD Y*, and (*e*) their ratio as a function of related label values, measured on the natural samples, $n = 1400$. A seemingly high data variance in (*d*), blue dots, was caused by smooth edges in DIW samples, but had a minor impact on the weighted accuracy due to a great difference between *X* and *Y* values.

$\varepsilon = 0$ than for IJP lines, as visible in Figure 7(*c*). In the whole, the line width was slightly underestimated. However, for both line types, corresponding points were located close to the area of ideal values. The same greater deviation from the ideal match is noticeable for DIW lines in Figure 7(*d*), where the *line-width variation Y* is considered. For both line types, the variation values were mostly overestimated—the stronger, the smoother line edges were. Yet, due to a different scale in Figures 7(*c*) and (*d*), represented data are not directly comparable, and the base effect has to be treated. For this purpose, we evaluated the measurement error in the *ratio Y to X*, depicted in Figure 7(*e*). Although related values for DIW lines were distributed farther from the *ideal match* $\varepsilon = 0$ than IJP lines, the measurement error remained in total below 10%, that also conformed to the smoothness factor for both line types (see Figure 7(*b*)). As well, the aforementioned insignificance of the reference value Y_L in relation to X_L is well distinguishable for DIW lines in Figure 7(*e*).

As expected, three optical-measurement techniques to collect label values provided slightly unequal results, as reported in Table 3 and represented in Figure 8(*a*). The measurement *congruence* among them was about 97.3%. Due to the applied image-binarization algorithm, the fully-automatic method had the highest measurement inaccuracy. The proposed algorithm demonstrated a comparable *congruence* of ∼98.3%. A drastic difference in the time cost was remarkable: the *average measurement time* was tens of seconds per single measurement for methods using manual operations, and tenth of a second for fully-automatic methods. Our algorithm was significantly faster than the common techniques, but yielded in accuracy. Yet, after value correction with respect to the NN-measurement error, the proposed method remained comparable to the fully-automatic one, overperforming it to a small extent.

Table 3. Measurement accuracy depending on the measurement method and exemplary natural sample.

Measurement method		Manual	Semi-automatic	Automatic	Proposed
Measuring equipment		Digital microscope	Optical profilometer	Optical probe station	Neural network
Number of measurements, for DIW/IJP samples		12/11	15/9	120/120	5/5
Average measurement time [s per sample]		42	20	0.3	0.14
			Per single measurement		Per image
Measured line width [µm]	DIW sample	235.91 ± 3.78	236.93 ± 4.78	244.19 ± 41.22	240.82 ± 15.49*
	IJP sample	273.58 ± 7.40	275.67 ± 8.39	286.75 ± 60.57	273.47 ± 25.61*
Result congruence [%]		97.33 ± 1.55			98.25 ± 1.44

*Not corrected Y_L values, measured and recorded by the NN without respect to the measurement errors.

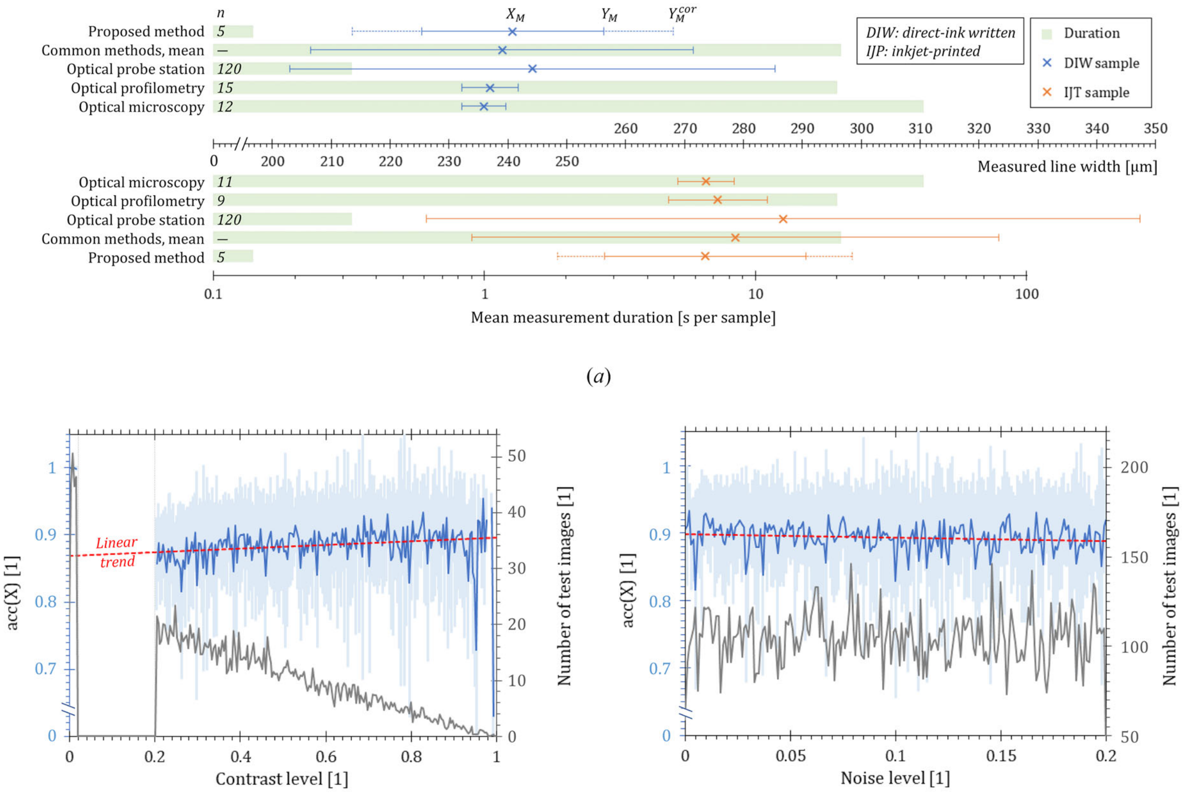

(a)

(b) (c)

Figure 8. (*a*) Measurement results and duration for the same individually-selected printed lines, depending on the measurement method. (*b*,*c*) Mean measurement accuracy and its linear trend on the synthetic test dataset, depending on (*b*) the contrast level, and (*c*) the noise level of the image, $n = 5000$. In (*b*): no test images related to the contrast levels between 0.02 and 0.2 were generated to avoid NN ambiguity during its training. A constantly decreasing number of test images was caused by the image-generation algorithm.

Typically for optical-measurement techniques, the image quality affected algorithm performance. In Figure 8(*b*), on the base of synthetic dataset, a clear positive correlation between the image *contrast level*, and the *measurement accuracy for the line width X* is noticeable. Hence, more contrast images with more clear object edges are expected to be assessed more precisely via ML. A large variability on the right-hand side of the diagram was caused by only few test images. In turn, that resulted from the image-generation algorithm. In Figure 8(*c*), a minor negative correlation between the image *noise level*, and the same *accuracy* as in Figure 8(*b*) is detectable. Indeed, noise and blur reduce clarity of the object edges in an image, and, hence, equivalently reduce the perceived image contrast.

4. Discussion

The literature survey performed revealed three major matters toward integration of ML into measuring applications in engineering. That were (a) complexity of the training-data collection, (b) high time and labor costs during the collection, and (c) an incommensurably low result quality. With the novel approach presented in this work, we addressed all the factors in combination. Thus, a tedious collection of the training samples from the real world was substituted with their digital generation. In turn, such process transformation shifts required preparatory stages from the real world into the digital area. That enabled a significant acceleration in the data preparation, an improved data variability, tailored to desired data assessments, and an improved integration with cyber-physical systems. As a result, the amount and complexity of preparatory manual operations and supplementary steps—such as preparation, enhancement, filtering, evaluation, and measurement of collected natural data—decrease, causing a drastic cost reduction. In particular, generation of a 1000 training images needed <3 min in our case, in comparison to at least few hours, if not days or even weeks by the conventional approach. An added benefit is an ability to create a manifold dataset, which is crucial for an efficient model training.

We achieved the measuring time of 140 ms per object image that was up to 3600 times faster than three conventional measurement methods. The requisite neural-net training duration of 6 ms/(epoch·image) did not exceed any critical level. Concurrently, accuracy of the conducted measurements was comparable with the chosen methods. Although genuine metrological approaches remain more reliable for the engineering community, a little less precise, but rapid and flexible property estimation of fabricated items is more advantageous under certain circumstances. Among them, a continuous inline process monitoring, difficult measurement conditions, a high level of the object and data inhomogeneity, variability in required measurands, and the need to simultaneously characterize multiple measurands have to be highlighted. In the view of the above, the proposed approach seems to be equipollent to the classic optical-measurement techniques.

As a whole, the results obtained proved a general applicability of the DL-based approach for a real-object measurement using fully-synthetic training data. We achieved the overall mean measurement accuracy of $91.7 \pm 8.3\%$ and demonstrated that common measuring methods are not completely precise as well. Analogous results were reported by Baderot et al.,[22] utilized automatically annotated natural objects for the NN training. Hence, despite previously reported concerns about feasibility of the ML-driven measurement tools in various engineering fields,[2–5,26] we confirmed potential prospects of such approach. The proposed algorithm is possible to transfer in a variety of applications, where a fully-automatic measurement of a large number of objects is desired, but collecting of appropriate training samples is challenging. In particular, this is true for construction engineering, agriculture and forestry, geoscience, health care, and micro and nano fabrication. Depending on one's need, further implicit measurands are likely to be concerned, such as frequency or ellipsoidality of an object shape, textural properties of a surface, layer thickness, etc. This implies a mere generation of an appropriate synthetic dataset, with no alterations in the neural-net architecture.

A major limiting factor identified during our work was the image quality. Noisy and low-contrast images with unclear object edges gradually reduced the assessment accuracy. In a common approach, such images require an additional enhancement. However, application of DL algorithms facilitates data extraction from such low-quality images and their subsequent processing. Therefore, input-data analysis remains possible even under complex measurement conditions, such as insufficient or specific illumination, turbid atmosphere, or limited range of vision. Still, generation of a relevant training dataset, reflecting target parameters, remains crucial. In addition to the requisite design of the synthetic training data, a further improved NN architecture is key. For instance, segmentation of the input image or Bayesian optimization of the hyperparameters are potentially advantageous.

Along with that, straight-like edges (see *class 1* in Table 2) have a minimal width variance. Hence, the base effect has to be considered when assessing such objects in respect to the *SD* value. As we found, if unsure, the NN tended to overestimate *SD* value that made measurement results less accurate. Furthermore, result deviation had to be additionally corrected with respect to the measurement inaccuracy. As it was expected, the IJP lines with their contrast and clear edges provided a reliable accuracy of ~94% for the line width and 60% for its variance, whereas less distinct DIW lines only 91 and 26%, correspondingly. Despite seemingly low accuracy values, the absolute value of the variance was mostly insignificantly small. It resulted in ca. one percentage-point less weighted accuracy, considering both line width and its deviation. In the whole, we achieved the target accuracy of over 90% for all target measurands, except for the *SD* values due to the strong base effect.

5. Conclusions and future work

We developed and analyzed a simple deep-learning-based algorithm to simultaneously quantify multiple measurands of natural objects using fully-synthetic training data. In contrast to state-of-the-art publications, a fast and uncomplicated data collection process was demonstrated for the first time. A substantial measurement accuracy of over 90% was attained, comparable with previously reported results on more sophisticated models. This enables application prospects of our algorithm in practical terms. Some additional factors affecting the results and demanding further elaboration were detected, such as image contrast and quality, and the edge shape.

In this paper, primary results of an ongoing research have been reported. In future work, we intend to elaborate the proposed method to expand our understanding of its applicability. In this process, an analysis of affecting and limiting factors, implementation of more sophisticated network architectures, transition to more complex object geometries, and increase in the algorithm robustness are envisaged.

Acknowledgments

The authors are grateful to Richard Thelen, Institute of Microstructure Technology, Karlsruhe Institute of Technology (KIT), for his consulting support in the field of metrological terms.

Disclosure statement

No potential conflict of interest was reported by the author(s).

Funding

This work was funded by the program Material Systems Engineering of the Helmholtz Association. Open access funding enabled and organized by Project DEAL.

References

[1] Polomoshnov, M.; Reichert, K.-M.; Rettenberger, L.; Ungerer, M.; Hernandez-Sosa, G.; Gengenbach, U.; Reischl, M. Image-Based Identification of Optical Quality and Functional Properties in Inkjet-Printed Electronics Using Machine Learning. *J. Intell. Manuf.* **2025**, *36*, 2709–2726. DOI: 10.1007/s10845-024-02385-4.

[2] Tercan, H.; Meisen, T. Machine Learning and Deep Learning Based Predictive Quality in Manufacturing: A Systematic Review. *J. Intell. Manuf.* **2022**, *33*, 1879–1905. DOI: 10.1007/s10845-022-01963-8.

[3] Zhang, L.; Shao, S. Image-Based Machine Learning for Materials Science. *J. Appl. Phys.* **2022**, *132*, 100701. DOI: 10.1063/5.0087381.

[4] Vallejo, M.; de la Espriella, C.; Gómez-Santamaría, J.; Ramírez-Barrera, A. F.; Delgado-Trejos, E. Soft Metrology Based on Machine Learning: A Review. *Meas. Sci. Technol.* **2020**, *31*, 032001. DOI: 10.1088/1361-6501/ab4b39.

[5] Zuo, C.; Qian, J.; Feng, S.; Yin, W.; Li, Y.; Fan, P.; Han, J.; Qian, K.; Chen, Q. Deep Learning in Optical Metrology: A Review. *Light. Sci. Appl.* **2022**, *11*, 39. DOI: 10.1038/s41377-022-00714-x.

[6] Balani, S. B.; Ghaffar, S. H.; Chougan, M.; Pei, E.; Şahin, E. Processes and Materials Used for Direct Writing Technologies: A Review. *Results Eng.* **2021**, *11*, 100257. DOI: 10.1016/j.rineng.2021.100257.

[7] Rau, D. A.; Williams, C. B.; Bortner, M. J. Rheology and Printability: A Survey of Critical Relationships for Direct Ink Write Materials Design. *Prog. Mater. Sci.* **2023**, *140*, 101188. DOI: 10.1016/j.pmatsci.2023.101188.

[8] Saadi, M. S. R.; Maguire, A.; Pottackal, N. T.; Thakur, M. S. H.; Ikram, M. M.; Hart, A. J.; Ajayan, P. M.; Rahman, M. M. Direct Ink Writing: A 3D Printing Technology for Diverse Materials. *Adv. Mater.* **2022**, *34*, e2108855. DOI: 10.1002/adma.202108855.

[9] Shah, M. A.; Lee, D.-G.; Lee, B.-Y.; Hur, S. Classifications and Applications of Inkjet Printing Technology: A Review. *IEEE Access* **2021**, *9*, 140079–140102. DOI: 10.1109/ACCESS.2021.3119219.

[10] Md Ashif, N. R.; Gengenbach, U.; Sieber, I. Process Development for Digital Fabrication of Radio Frequency Transmission Lines with off-the-Shelf Equipment. In *2024 Symposium on Design, Test, Integration and Packaging of MEMS/MOEMS (DTIP)*; 2024; pp 1–5. DOI: 10.1109/DTIP62575.2024.10613213.

[11] Sieber, I.; Thelen, R.; Gengenbach, U. Assessment of High-Resolution 3D Printed Optics for the Use Case of Rotation Optics. *Opt. Express* **2020**, *28*, 13423–13431. DOI: 10.1364/OE.391697.

[12] Kipphan, H. *Handbook of Print Media*; Berlin, Heidelberg: Springer, 2001.

[13] Roach, D. J.; Rohskopf, A.; Leguizamon, S.; Appelhans, L.; Cook, A. W. Invertible Neural Networks for Real-Time Control of Extrusion Additive Manufacturing. *Addit. Manuf.* **2023**, *74*, 103742. DOI: 10.1016/j.addma.2023.103742.

[14] Leach, R.; Giusca, C. Calibration of Optical Surface Topography Measuring Instruments. In *Optical Measurement of Surface Topography*; Berlin, Heidelberg: Springer, 2011; pp 49–70.

[15] Mayinger, F.; Feldmann, O. Introduction. In *Optical Measurements: Techniques and Applications*; Berlin, Heidelberg: Springer, 2001; pp 1–4.

[16] Sirohi, R. S. *Optical Methods of Measurements: Wholefield Techniques*, 2nd ed.; Boca Raton, FL: CRC Press, 2009.

[17] Feldmann, O.; Tauscher, R. Evaluation of Holograms by Digital Image Processing. In *Optical Measurements: Techniques and Applications*; Berlin, Heidelberg: Springer, 2001; pp 79–84.

[18] Vukašinović, N.; Duhovnik, J. Optical 3D Geometry Measurements Based on Laser Triangulation. In *Advanced CAD Modeling*; Cham: Springer International Publishing, 2019; pp 191–216.

[19] Chai, J.; Zeng, H.; Li, A.; Ngai, E. W. T. Deep Learning in Computer Vision: A Critical Review of Emerging Techniques and Application Scenarios. *Mach. Learn. Appl.* **2021**, *6*, 100134. DOI: 10.1016/j.mlwa.2021.100134.

[20] Shimizu, Y.; Chen, L.-C.; Kim, D. W.; Chen, X.; Li, X.; Matsukuma, H. An Insight into Optical Metrology in Manufacturing. *Meas. Sci. Technol.* **2021**, *32*, 042003. DOI: 10.1088/1361-6501/abc578.

[21] Shpak, M.; Burger, S.; Byman, V.; Saastamoinen, K.; Haapalainen, M.; Lassila, A. Online Measurement of Optical Fibre Geometry during Manufacturing. In *Fiber Lasers and Glass Photonics: Materials through Applications*; SPIE, 2018; Vol. 10683, pp 180–185. DOI: 10.1117/12.2314762.

[22] Baderot, J.; Grould, M.; Misra, D.; Clément, N.; Hallal, A.; Martinez, S.; Foucher, J. Application of Deep-Learning Based Techniques for Automatic Metrology on Scanning and Transmission Electron Microscopy Images. *J. Vac. Sci. Technol. B* **2022**, *40*, 054003. DOI: 10.1116/6.0001988.

[23] Ratava, J.; Penttilä, S.; Lohtander, M.; Kah, P. Optical Measurement of Groove Geometry. *Procedia Manuf.* **2018**, *25*, 111–117. DOI: 10.1016/j.promfg.2018.06.064.

[24] Gao, W.; Shimizu, Y. *Optical Metrology for Precision Engineering*; De Gruyter: Berlin, 2022.

[25] Xing, Y.; Dong, J.; Dwivedi, S.; Khan, U.; Bogaerts, W. Accurate Extraction of Fabricated Geometry Using Optical Measurement. *Photon. Res.* **2018**, *6*, 1008–1020. DOI: 10.1364/PRJ.6.001008.

[26] Fan, Z.; Hu, X.; Gao, R. X. Indirect Measurement Methods for Quality and Process Control in Nanomanufacturing. *Nanomanuf. Metrol.* **2022**, *5*, 209–229. DOI: 10.1007/s41871-022-00148-4.

[27] Mahadevkar, S. V.; Khemani, B.; Patil, S.; Kotecha, K.; Vora, D. R.; Abraham, A.; Gabralla, L. A. A Review on Machine Learning Styles in Computer Vision—Techniques and Future Directions. *IEEE Access* **2022**, *10*, 107293–107329. DOI: 10.1109/ACCESS.2022.3209825.

[28] Rana, M.; Bhushan, M. Machine Learning and Deep Learning Approach for Medical Image Analysis: Diagnosis to Detection. *Multimed. Tools Appl.* **2022**, *82*, 1–39. DOI: 10.1007/s11042-022-14305-w.

[29] Münke, F. R.; Schützke, J.; Berens, F.; Reischl, M. A Review of Adaptable Conventional Image Processing Pipelines and Deep Learning on Limited Datasets. *Mach. Vis. Appl.* **2024**, *35*, 25. DOI: 10.1007/s00138-023-01501-3.

[30] Kuzin, A. Y.; Kroshkin, A. N.; Isaev, L. K.; Bulygin, F. V.; Voytko, V. D. Practical Aspects of Applying Artificial Intelligence in Metrology. *Meas. Tech.* **2023**, *66*, 717–727. DOI: 10.1007/s11018-024-02285-2.

[31] Liang, D.; Lu, J.; Wei, Y.; Nong, Y.; Lu, T.; Chen, Z.; Tan, M.; Zhong, Z. Real-Time Width Measurement Method of Cut Tobacco Based on Machine Vision for Industrial Applications. In *Fourth International Conference on Computer Science and Communication Technology (ICCSCT 2023)*; SPIE, 2023; Vol. 12918, pp 573–579. DOI: 10.1117/12.3009376.

[32] Ponnusamy, R.; Zhang, M.; Chang, Z.; Wang, Y.; Guida, C.; Kuang, S.; Sun, X.; Blackadar, J.; Driban, J. B.; McAlindon, T.; Duryea, J.; Schaefer, L.; Eaton, C. B.; Haugen, I. K.; Shan, J. Automatic Measuring of Finger Joint Space Width on Hand Radiograph Using Deep Learning and Conventional Computer Vision Methods. *Biomed. Signal Process. Control* **2023**, *84*, 104713. DOI: 10.1016/j.bspc.2023.104713.

[33] Carrasco, M.; Araya-Letelier, G.; Velázquez, R.; Visconti, P. Image-Based Automated Width Measurement of Surface Cracking. *Sensors* **2021**, *21*, 7534. DOI: 10.3390/s21227534.

[34] Lamouchi, D.; Yaddaden, Y.; Cherif, R.; Smaoui, A. A New Method of Crack Width Estimation for Concrete Structures Monitoring. In *2022 IEEE 21st International Ccnference on Sciences and Techniques of Automatic Control and Computer Engineering (STA)*; 2022; pp 336–341. DOI: 10.1109/STA56120.2022.10019132.

[35] Nyathi, M. A.; Bai, J.; Wilson, I. D. Deep Learning for Concrete Crack Detection and Measurement. *Metrology* **2024**, *4*, 66–81. DOI: 10.3390/metrology4010005.

[36] Tang, Y.; Huang, Z.; Chen, Z.; Chen, M.; Zhou, H.; Zhang, H.; Sun, J. Novel Visual Crack Width Measurement Based on Backbone Double-Scale Features for Improved Detection Automation. *Eng. Struct.* **2023**, *274*, 115158. DOI: 10.1016/j.engstruct.2022.115158.

[37] Shabani, A.; Martinez-Hernandez, U. *In-Situ* Measurement of Extrusion Width for Fused Filament Fabrication Process Using Vision and Machine Learning Models. In *2023 IEEE/RSJ International Conference on Intelligent Robots and Systems (IROS)*; 2023; pp 8298–8303. DOI: 10.1109/IROS55552.2023.10341406.

[38] Holm, E. A.; Cohn, R.; Gao, N.; Kitahara, A. R.; Matson, T. P.; Lei, B.; Yarasi, S. R. Overview: Computer Vision and Machine Learning for Microstructural Characterization and Analysis. *Metall. Mater. Trans. A* **2020**, *51*, 5985–5999. DOI: 10.1007/s11661-020-06008-4.

[39] Tin, T. C.; Tan, S. C.; Lee, C. K. Virtual Metrology in Semiconductor Fabrication Foundry Using Deep Learning Neural Networks. *IEEE Access* **2022**, *10*, 81960–81973. DOI: 10.1109/ACCESS.2022.3193783.

[40] Xue, R.; Hooshmand, H.; Isa, M.; Piano, S.; Leach, R. Applying Machine Learning to Optical Metrology: A Review. *Meas. Sci. Technol.* **2025**, *36*, 012002. DOI: 10.1088/1361-6501/ad7878.

[41] Bruch, R.; Vitacolonna, M.; Nürnberg, E.; Sauer, S.; Rudolf, R.; Reischl, M. Improving 3D Deep Learning Segmentation with Biophysically Motivated Cell Synthesis. *Commun. Biol.* **2025**, *8*, 43. DOI: 10.1038/s42003-025-07469-2.

[42] Orth, A.; Höfer, H.; Nefedov, A.; Jalali, M.; Wöll, C.; Reischl, M. ML-Based XPS Quantification Supported by Synthetic Dataset Generation. *Curr. Direc. Biomed. Eng.* **2024**, *10*, 482–485. DOI: 10.1515/cdbme-2024-2118.

[43] Polomoshnov, M.; M. D.; Ashif, N. R.; Reischl Natural and Synthetic Datasets for Rapid Deep-Learning-Based Optical Measurement of Printed Linear Structures. Repositary KITopen; 2025. 10.35097/kf4tg7xk649w984q.

[44] Polomoshnov, M.; M. D.; Ashif, N. R.; Reischl, M. Extended Natural Dataset for Rapid Deep-Learning-Based Optical Measurement of Printed Linear Structures. Repositary KITopen; 2025. 10.35097/vc8pdwnszx58uknz.

[45] Kenton, W. *What Is the Base Effect? Definition and How Comparison Works*; Investopedia, 2013. https://www.investopedia.com/terms/b/base-effect.asp.

[46] Kohn, W.; Öztürk, R. *Statistik Für Ökonomen [Statistics for Economists]*, 3rd ed.; Berlin, Heidelberg: Springer Gabler, 2022.

[47] Czichos, H. Introduction to Metrology and Testing. In *Springer Handbook of Metrology and Testing*; Berlin, Heidelberg: Springer, 2011; pp 1–22.

[48] Gengenbach, U.; Ungerer, M.; Koker, L.; Reichert, K.-M.; Stiller, P.; Allgeier, S.; Köhler, B.; Zhu, X.; Huang, C.; Hagenmeyer, V. Automated Fabrication of Hybrid Printed Electronic Circuits. *Mechatronics* **2020**, *70*, 102403. DOI: 10.1016/j.mechatronics.2020.102403.